Aspect-ratio-dependent void formation in active rhomboidal and elliptical particle systems

Motoya Suzaka, Hiroaki Ito, and Hiroyuki Kitahata*
Department of Physics, Chiba University, Chiba 263-8522, Japan
(Dated: February 2, 2023)

We execute a numerical simulation on active nematics with particles interacting by excluded volume effect. The system with rhomboidal particles and that with elliptical particles are considered in order to investigate the effect of the direct contact of particles. In our simulation, the void regions, where the local number density is almost zero, appear in both the systems when aspect ratio of the particles is high. We focused on the relationship between the void regions and the particle orientation of the bulk. The particle number density, particle orientation, topological defects, and void regions are analyzed for different aspect ratios in both the systems. The systems with rhomboidal particles have a characteristic void size, which increases with an increase in the aspect ratio. In contrast, the distribution of the void-region size in the systems with elliptical particles is broad. The present results suggest that the void size in the system with rhomboidal particles is determined by the correlation length of the particle orientational field around the void regions, while that in the system with elliptical particles might be determined by the system size.

I. INTRODUCTION

Active matter consists of particles that propel themselves using free energy[1–3]. It has been reported that characteristic phenomena originating from collective motions such as giant number fluctuations (GNF)[4–6] and motility-induced phase separation (MIPS)[7–10] appear in active matter systems. Active matter can be classified into several classes with respect to the symmetry of the particles; scalar, polar, nematic, and chiral active matter[11]. Scalar active matter consists of isotropic active particles that interact each other depending only on the distance between the particles. The active behavior induces the breakage of spatial symmetry, which often appears as MIPS and GNF[12–15]. Polar active matter consists of self-propelled particles with head-tail asymmetry. Some systems, which consist of animals, microswimmers, and Janus particles, are recognized as polar active matter[16–19]. Vicsek model is one of the most studied models for polar active matter, in which non-equilibrium phase transition occurs between the isotropic and polar states[20, 21]. Active nematics are systems with particles interacting with each other by dyad rotational symmetry and have been studied in both experiments and numerical simulations[22]. Microtubules driven by motor proteins on substrates[23–26], colonies of rod-like bacteria[27–31], and elongated cells in tissues[32–35] are the typical examples of active nematics. Chiral active matter is the systems with particles with mirror-image asymmetry, in which chiral collective motions often appear. Designed self-propelled granular ellipsoids, chiral liquid colloids, spermatozoa, and pea-shaped Quincke rollers are investigated as chiral active matter[36–38].

In the present study, we focus on the active nematic system. In active nematics, particles often make locally aligned structures and inhomogeneous density distribution, which can be understood as orientational and density fields. Characteristic orientational patterns in these fields appear as vortices or bent bands with topological defects, i.e., singular points[24, 39, 40]. Topological defects are used to characterize the orientational pattern formation in many studies[41–43]. It was reported that the topological defects with sustainable movements based on particle activity break the long-range nematic order and lead spatio-temporal dynamics of the orientational patterns[44–46]. The emergence of typical density patterns has been reported in active nematics; In low-density systems, clustering and phase separation are exhibited [47–50], and in high-density systems, topological defects cause the density inhomogeneity through the inflow or outflow of particles[51–55]. In a middle-density system, the void regions whose local particle number density is much lower than the mean of the whole system are observed. Shi and Ma simulated an active nematics system with elliptical particles and claimed that void regions are generated through the collision of two $+1/2$ topological defects[56].

In this study, we focus on the size of the void regions, which should be essential to determine the properties of the whole system. In particular, we are interested in whether the size of the void regions is determined by the system size or other properties of particles and bulk. The particle shape should be important to determine the size of void regions because particles interact by direct collisions. It was reported that the number and size of clusters are changed by the anisotropy of particle shapes[57, 58]. We simulate an active nematics model constructed based on the model by Shi and Ma[56]. We adopt the two different particle shapes, rhomboidal and elliptical particles, in order to investigate the effect of the difference in direct contact among particles. The aspect ratio of particles is changed as a parameter to check the effect of the magnitude of the nematic interaction. The local nematic order, the area of void regions, and wind-

* kitahata@chiba-u.jp

ing numbers of topological defects are analyzed. Through these analyses, the possible relation between the characteristic void size and the orientational structure of the void regions is discussed with geometrical consideration.

The paper consists of the sections as follows. In Sec. II, we explain the methods of the simulation and the data analyses. In Sec. III, we show the results of the numerical simulation, focusing on the particle-shape dependence in the local number density, the local orientation, the topological defects, and the void regions. In Sec. IV, we discuss the mechanism to determine the characteristic size of void regions, considering the orientational structure around the void regions. In Sec. V, We summarize our study.

II. METHOD

A. Simulation model

We consider a two-dimensional squared system with a periodic boundary condition, where the length of the sides is $L^{(\mathrm{sys})}$ and the area is thus $(L^{(\mathrm{sys})})^2$. The system includes N self-propelled nematic particles with the same shapes. As the shape of the nematic particles, two cases, i.e., rhomboid or ellipse, are considered. We set $\boldsymbol{x}_{i,t}$ to be the coordinates of the center of mass of the i-th ($i = 1, \ldots, N$) particle at a discrete time step t, and $\theta_{i,t}$ to be the angle of the traveling direction, which meets one of the two long-axis directions of the particle. We also introduce the variable $\Lambda_{i,t}$, which represents the memory on the overlap with other particles at the last step.

The dynamics of the particles is described as follows. The particles interact with each other only by the excluded volume effect. The trial motion is described with a tentative position $\boldsymbol{x}'_{i,t}$ and angle $\theta'_{i,t}$ as

$$\boldsymbol{x}'_{i,t} = \boldsymbol{x}_{i,t} + \eta_i^{(t)} D^{(t)} \boldsymbol{e}\left(\theta'_{i,t}\right) + \Lambda_{i,t} D^{(r)} \eta_{i,t}^{(r)} \boldsymbol{e}\left(2\pi\eta_{i,t}^{(\varphi)}\right), \tag{1}$$

$$\theta'_{i,t} = \theta_{i,t} + \pi\zeta_{i,t} + \Lambda_{i,t}\pi D^{(\theta)}\eta_{i,t}^{(\theta)}, \tag{2}$$

and then the overlap of the particle at $\boldsymbol{x}'_{i,t}$ and $\theta'_{i,t}$ with the other particles is checked. The trial motion is rejected if overlap is detected, while it is accepted if overlap is not detected. In other words, the position, the angle, and the memory at the next time step are determined as

$$\begin{aligned}&(\boldsymbol{x}_{i,t+1},\ \theta_{i,t+1},\ \Lambda_{i,t+1})\\ &= \begin{cases} (\boldsymbol{x}_{i,t},\ \theta_{i,t},\ 1), & \text{if overlaps are detected at the trial,}\\ (\boldsymbol{x}'_{i,t},\ \theta'_{i,t},\ 0), & \text{otherwise.}\end{cases}\end{aligned} \tag{3}$$

Here, $\eta_i^{(t)}$, $\eta_{i,t}^{(r)}$, $\eta_{i,t}^{(\varphi)}$ and $\eta_{i,t}^{(\theta)}$ are stochastic variables that obey the uniform distribution in $[0, 1]$ for $\eta_i^{(t)}$, $\eta_{i,t}^{(r)}$, and $\eta_{i,t}^{(\varphi)}$, and in $[-1, 1]$ for $\eta_{i,t}^{(\theta)}$. $D^{(t)}$ is the maximum distance of the motion in the travelling direction of the particle. $D^{(r)}$ and $D^{(\theta)}$ are the maximum distance of the motion in a random direction and the maximum angle of a random rotation over π, respectively, in the case that the overlap is detected at the last time step. $\boldsymbol{e}(\theta) = (\cos\theta, \sin\theta)$ is a unit vector in the direction of θ. $\zeta_{i,t}$ is a stochastic variable representing the switching of the travelling direction with a characteristic time τ,

$$\zeta_{i,t} = \begin{cases} 1, & \text{probability of } 1/\tau,\\ 0, & \text{probability of } 1 - 1/\tau.\end{cases} \tag{4}$$

In this study, the aspect ratio of the particle a is varied from 1.5 to 6.0 as a paramenter under the constraint that the particle area s is constant and common for rhomboidal and elliptical particles. That is to say, the long-axis lengths $l^{(\mathrm{r})}$ and $l^{(\mathrm{e})}$ for rhomboidal and elliptical particles are determined by $s = (l^{(\mathrm{r})})^2/(2a)$, and $s = \pi(l^{(\mathrm{e})})^2/(4a)$. The area of the particles is fixed to be $s = \pi/23$. The other parameters are fixed as $N = 4140$, $L^{(\mathrm{sys})} = 30$, $D^{(t)} = 0.012$, $D^{(r)} = 0.004$, $D^{(\theta)} = 0.015$, and $\tau = 6$. The time evolution processes are repeated up to the maximum time step $t = 2 \times 10^7$. Ten times numerical simulations are performed for each parameter set, with different initial conditions and different stochastic noise series. Statistic quantities are calculated from the data every 10^4 time step for $t \geq 1 \times 10^7$ in the ten numerical results.

B. Data Analysis

To measure the local number density, the local nematic order, and the local mean orientation, $M_x \times M_y$ measurement points are set on a regular grid, where M_x and M_y are even numbers and we set $M_x = M_y = 64$ in the present analysis. The measurement point is indexed as $\boldsymbol{j} = (j_x, j_y)$ ($j_x = 1, \ldots, M_x$; $j_y = 1, \ldots, M_y$), and the positional vector of the measurement point is $\boldsymbol{y}_{\boldsymbol{j}} = (L^{(\mathrm{sys})} j_x/M_x, L^{(\mathrm{sys})} j_y/M_y)$.

Under a given particle configuration $\{\boldsymbol{x}_{i,t}\}$, local number density $\rho_{\boldsymbol{j},t}$ at the measurement point $\boldsymbol{j}$ at the time step t is defined as

$$\begin{aligned}\rho_{\boldsymbol{j},t} &= \frac{\int \sum_{i=1}^{N} \delta(\boldsymbol{r} - \boldsymbol{x}_{i,t}) W(\boldsymbol{r} - \boldsymbol{y}_{\boldsymbol{j}}) d\boldsymbol{r}}{\int W(\boldsymbol{r} - \boldsymbol{y}_{\boldsymbol{j}}) d\boldsymbol{r}}\\ &= \frac{\sum_{i=1}^{N} W(\boldsymbol{x}_{i,t} - \boldsymbol{y}_{\boldsymbol{j}})}{\int W(\boldsymbol{r} - \boldsymbol{y}_{\boldsymbol{j}}) d\boldsymbol{r}}.\end{aligned} \tag{5}$$

Here, $W(\boldsymbol{r})$ is a kernel function

$$W(\boldsymbol{r}) = \begin{cases} 0, & |\boldsymbol{r}| > 1,\\ 1 - |\boldsymbol{r}|, & |\boldsymbol{r}| \leq 1,\end{cases} \tag{6}$$

and $\delta(\cdot)$ represents the Dirac's delta function.

The local nematic order $P_{\boldsymbol{j},t}$ at the measurement point $\boldsymbol{j}$ at the time step t is defined as

$$P_{\boldsymbol{j},t} = \left|\det Q_{\boldsymbol{j},t}\right|. \tag{7}$$

Here, $Q_{\boldsymbol{j},t}$ is defined as

$$Q_{\boldsymbol{j},t} = \begin{pmatrix} H^{(\cos)}_{\boldsymbol{j},t} & H^{(\sin)}_{\boldsymbol{j},t} \\ H^{(\sin)}_{\boldsymbol{j},t} & -H^{(\cos)}_{\boldsymbol{j},t} \end{pmatrix}, \tag{8}$$

where

$$H^{(\cos)}_{\boldsymbol{j},t} = \frac{\int \sum_{i=1}^{N} \delta(\boldsymbol{r} - \boldsymbol{x}_{i,t}) W(\boldsymbol{r} - \boldsymbol{y}_{\boldsymbol{j}}) \cos 2\theta_{i,t}\, d\boldsymbol{r}}{\int W(\boldsymbol{r} - \boldsymbol{y}_{\boldsymbol{j}})\, d\boldsymbol{r}} = \frac{\sum_{i=1}^{N} W(\boldsymbol{x}_{i,t} - \boldsymbol{y}_{\boldsymbol{j}}) \cos 2\theta_{i,t}}{\int W(\boldsymbol{r} - \boldsymbol{y}_{\boldsymbol{j}})\, d\boldsymbol{r}}, \tag{9}$$

and

$$H^{(\sin)}_{\boldsymbol{j},t} = \frac{\int \sum_{i=1}^{N} \delta(\boldsymbol{r} - \boldsymbol{x}_{i,t}) W(\boldsymbol{r} - \boldsymbol{y}_{\boldsymbol{j}}) \sin 2\theta_{i,t}\, d\boldsymbol{r}}{\int W(\boldsymbol{r} - \boldsymbol{y}_{\boldsymbol{j}})\, d\boldsymbol{r}} = \frac{\sum_{i=1}^{N} W(\boldsymbol{x}_{i,t} - \boldsymbol{y}_{\boldsymbol{j}}) \sin 2\theta_{i,t}}{\int W(\boldsymbol{r} - \boldsymbol{y}_{\boldsymbol{j}})\, d\boldsymbol{r}}. \tag{10}$$

The local mean orientation $\phi_{\boldsymbol{j},t}$ at the measurement point $\boldsymbol{j}$ at the time step t is defined as

$$H_0 e^{2\sqrt{-1}\phi_{\boldsymbol{j},t}} = H^{(\cos)}_{\boldsymbol{j},t} + \sqrt{-1} H^{(\sin)}_{\boldsymbol{j},t}, \quad (H_0 > 0). \tag{11}$$

It should be noted that $\phi_{\boldsymbol{j},t}$ cannot be defined at the measurement points with $H^{(\cos)}_{\boldsymbol{j},t} = H^{(\sin)}_{\boldsymbol{j},t} = 0$.

Next, to characterize topological defects and void regions, $(M_x/2) \times (M_y/2)$ coarse measurement points are set on a regular grid. The coarse measurement point is indexed as $\boldsymbol{k} = (k_x, k_y)$ $(k_x = 1, \ldots, (M_x/2); k_y = 1, \ldots, (M_y/2))$, and the positional vector of the coarse measurement point is $\boldsymbol{z}_{\boldsymbol{k}} = (2L^{(\mathrm{sys})}k_x/M_x, 2L^{(\mathrm{sys})}k_y/M_y)$. It should be noted that $\boldsymbol{y}_{2\boldsymbol{k}} = \boldsymbol{z}_{\boldsymbol{k}}$ holds.

A coarse measurement point indexed by $\boldsymbol{k}$ is called as a "void point" if the minimum of the nine values $\rho_{\boldsymbol{j},t}$ for $j_x = 2k_x, 2k_x \pm 1$ and $j_y = 2k_y, 2k_y \pm 1$ is less than $0.3\rho^{(\mathrm{sys})}$, where $\rho^{(\mathrm{sys})} = N/(L^{(\mathrm{sys})})^2$. A "void region" is defined as the eight-neighboring connected "void points". The number of void regions at the time step t is represented as $\mathcal{N}^{(\mathrm{void})}_t$. The area of the m-th void region at the time step t is defined as $S^{(\mathrm{void})}_{m,t} = \chi_{m,t}(L^{(\mathrm{sys})})^2/(M_x M_y/4)$ $(m = 1, \ldots, \mathcal{N}^{(\mathrm{void})}_t)$, where $\chi_{m,t}$ is the number of void points belonging to the m-th void region. The mean area of void regions weighted by the void region area at the time step t is defined as

$$\bar{S}^{(\mathrm{void})}_t = \frac{\sum_m (S^{(\mathrm{void})}_{m,t})^2}{\sum_m S^{(\mathrm{void})}_{m,t}}. \tag{12}$$

Then, $\left\langle \bar{S}^{(\mathrm{void})} \right\rangle$ is defined as the mean of $\bar{S}^{(\mathrm{void})}_t$ with respect to t and the ten trials.

The winding number $\Phi_{\boldsymbol{k},t}$ at the coarse measurement point indexed by $\boldsymbol{k}$ is calculated as follows. First, the indices of the surrounding eight measurement points around the focused coarse measurement point are set as $\boldsymbol{j} = \boldsymbol{J}^{(\boldsymbol{k})}_1, \ldots, \boldsymbol{J}^{(\boldsymbol{k})}_8$, so that these points surround the focused coarse measurement point counterclockwise. We calculate the local orientation difference as

$$\Delta\phi^{(\boldsymbol{k})}_{\ell,t} = \phi_{\boldsymbol{J}^{(\boldsymbol{k})}_{\ell},t} - \phi_{\boldsymbol{J}^{(\boldsymbol{k})}_{\ell-1},t}, \quad (-\frac{\pi}{2} < \Delta\phi^{(\boldsymbol{k})}_{\ell,t} < \frac{\pi}{2}), \quad (\ell = 1, ..., 8). \tag{13}$$

Then, the winding number is calculated as

$$\Phi_{\boldsymbol{k},t} = \frac{1}{2\pi} \sum_{\ell=1}^{8} \Delta\phi^{(\boldsymbol{k})}_{\ell,t}. \tag{14}$$

Here, it should be noted that we set $\boldsymbol{J}^{(\boldsymbol{k})}_0 = \boldsymbol{J}^{(\boldsymbol{k})}_8$.

The winding number $\Psi_{m,t}$ of the void region indexed by m at the time step t is calculated almost in the same manner. The indices of the surrounding measurement points around the m-th void region are set as $\boldsymbol{j} = \boldsymbol{J}^{(m,t)}_1, \ldots, \boldsymbol{J}^{(m,t)}_{\nu_{m,t}}$, so that these points surround the void region counterclockwise. Here, $\nu_{m,t}$ is the number of the surrounding measurement points around the m-th void region. Then, we calculate the local orientation difference as

$$\Delta\psi^{(m,t)}_{h,t} = \phi_{\boldsymbol{J}^{(m,t)}_{h},t} - \phi_{\boldsymbol{J}^{(m,t)}_{h-1},t}, \quad (-\frac{\pi}{2} < \Delta\psi^{(m)}_{h,t} < \frac{\pi}{2}), \quad (h = 1, ..., \nu_{m,t}). \tag{15}$$

The winding number is calculated as

$$\Psi_{m,t} = \frac{1}{2\pi} \sum_{h=1}^{\nu_{m,t}} \Delta\psi^{(m,t)}_{h,t}. \tag{16}$$

Here, it should be noted that we set $\boldsymbol{J}^{(m,t)}_0 = \boldsymbol{J}^{(m.t)}_{\nu_{m,t}}$. For the calculation of $\Psi_{m,t}$, islands of the coarse measurement points with $\rho_{\boldsymbol{j},t} \geq 0.3\rho^{(\mathrm{sys})}$ inside of void regions are ignored, and only the coarse measurement points along the outer boundaries of the void regions are considered.

III. RESULTS

Figure 1 shows the results of the numerical simulation. Snapshots at $t = 1.9 \times 10^7$ for the systems with rhomboidal and elliptical particles, with the aspect ratios $a = 3.0$, 4.0, and 5.0 are shown in Figs. 1(a,b). Figures 1(c-f) show the corresponding local number density $\rho_{\boldsymbol{j},t}/\rho^{(\mathrm{sys})}$ (c,d), and the local nematic order $P_{\boldsymbol{j},t}$ (e,f). Both in the systems with rhomboidal and elliptical particles, the void regions that are shown as the white regions in Figs. 1(e,f) are observed for the higher aspect ratio. In addition, the particles are more aligned for the higher aspect ratio as shown in Fig. 1(e,f). The void regions are observed for rhomboidal particles with $a = 4.0$ and 5.0 and elliptical particles with $a = 5.0$. Multiple small void regions are observed in the systems with rhomboidal particles, while a single large void region is observed in the systems with elliptical particles. Fig-

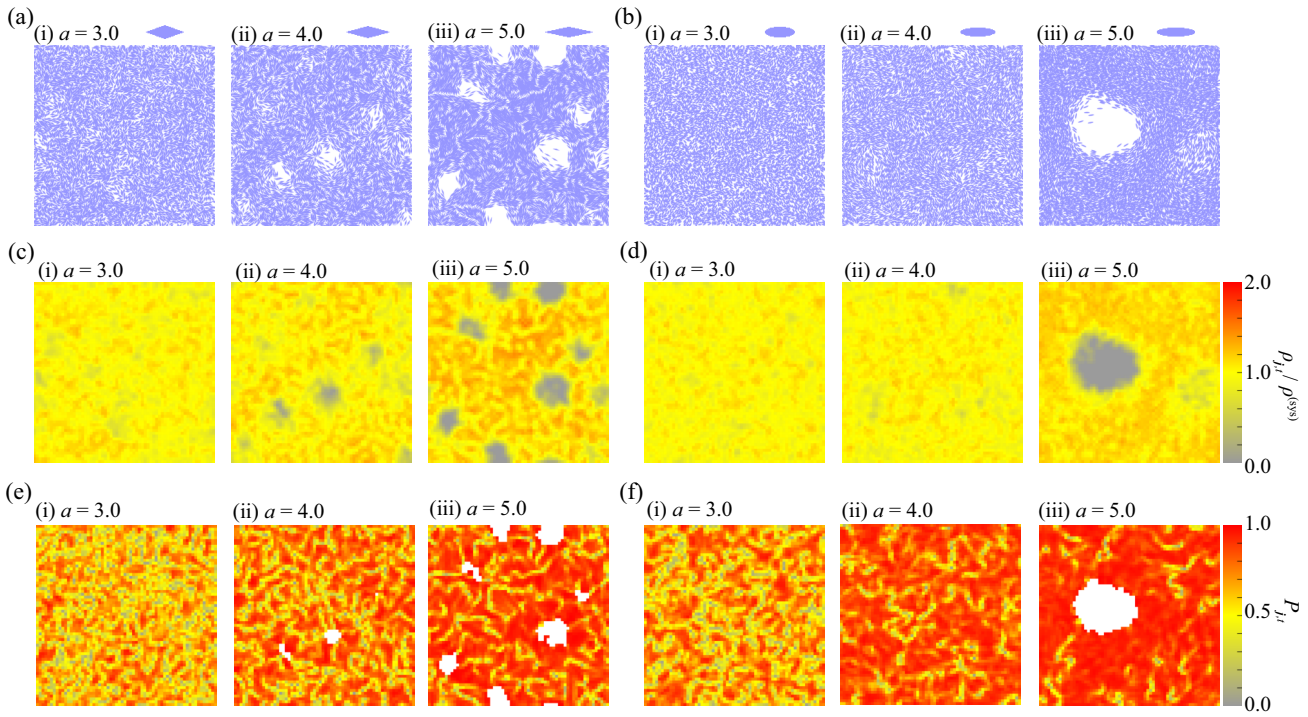

FIG. 1. Representative results of the numerical simulations for the system with (a,c,e) rhomboidal and (b,d,f) elliptical particles at $t = 1.9 \times 10^7$. Aspect ratio is (i) $a = 3.0$, (ii) $a = 4.0$, and (iii) $a = 5.0$. (a,b) Snapshots. The particle shape is illustrated on the upper side. (c,d) Local number density $\rho_{\boldsymbol{j},t}/\rho^{(\mathrm{sys})}$. (e,f) Local nematic order $P_{\boldsymbol{j},t}$, where white areas indicate the void regions in (e,f).

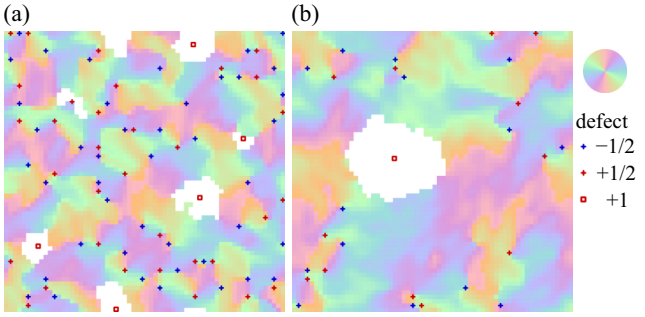

FIG. 2. The local mean orientations $\phi_{j,t}$ with the positions of the topological defects in the systems with (a) rhomboidal and (b) elliptical particles for $a = 5.0$ at $t = 1.9 \times 10^7$. White areas indicate the void regions.

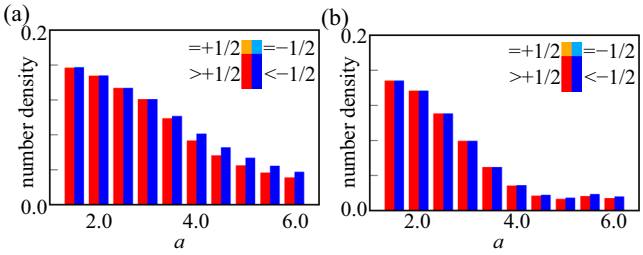

FIG. 3. Number density of the topological defects depending on the aspect ratio a for the system with (a) rhomboidal and (b) elliptical particles. The colors indicate the winding numbers. The fractions of the defects with winding numbers more than $+1/2$ or less than $-1/2$ are too small to recognize.

ures 2(a,b) show the local mean orientations $\phi_{j,t}$ with the positions of the topological defects in the systems with rhomboidal (a) and elliptical (b) particles for $a = 5.0$. In these representative results, topological defects appear with $\Phi_{\boldsymbol{k},t} = \pm 1/2$ and the void regions appear with $\Psi_{m,t} = +1$.

Figure 3 shows the number density of defects depending on the aspect ratio a for both the systems with rhomboidal and elliptical particles. It decreases with an increase in a, and the systems with rhomboidal particles include more defects than those with elliptical particles for the same aspect ratio. Almost all topological defects have the winding number $\Phi_{\boldsymbol{k},t} = +1/2$ or $-1/2$, and the defects with the winding numbers more than $+1/2$ or less than $-1/2$ are rarely observed. Figure 4 shows the number density of void regions with various winding numbers for both in the systems with rhomboidal and elliptical particles. Void regions are not observed for $a \leq 3$ in the systems with rhomboidal particles and for $a \leq 4$

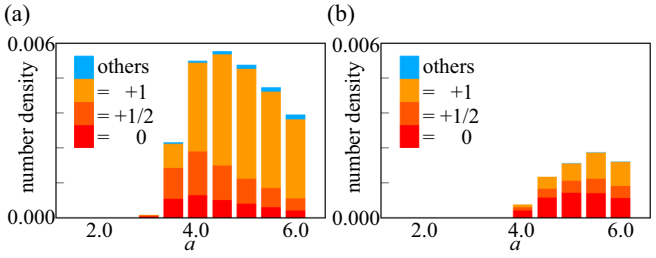

FIG. 4. Number density of the void regions depending on the aspect ratio a for the systems with (a) rhomboidal and (b) elliptical particles. The colors indicate winding numbers.

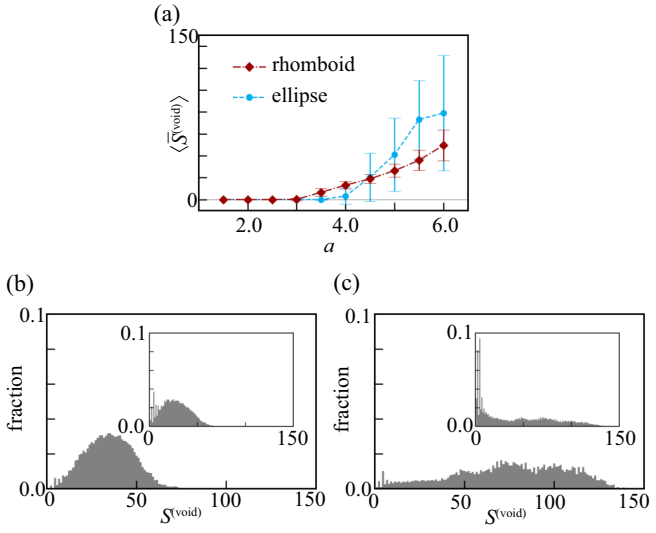

FIG. 5. (a) Ten times ensemble and time average of the void area $\left\langle \bar{S}^{(\mathrm{void})} \right\rangle$. Error bars indicate standard deviation in (a). Histogram of the void area $S^{(\mathrm{void})}$ for the systems with (b) rhomboidal and (c) elliptical particles. Aspect ratio is $a = 5.0$. The fraction is taken with weighting by the void region $S^{(\mathrm{void})}$. The fraction with respect to the count is shown in the inset.

in those with elliptical particles. Almost all void regions have the positive or zero winding numbers. The fraction of the winding number $+1$ increases with an increase in a. The void regions with the winding numbers over $+1$ are rarely observed and those with negative winding number are not observed.

Figure 5(a) shows the mean size of void regions $\left\langle \bar{S}^{(\mathrm{void})} \right\rangle$ against a for both the systems. $\left\langle \bar{S}^{(\mathrm{void})} \right\rangle$ increases with an increase in a for high aspect ratios both in the systems with rhomboidal and elliptical particles. In addition, for these a, the standard deviation of $\bar{S}^{(\mathrm{void})}$ in the system with rhomboidal particles is smaller than that in the system with elliptical particles. The distribution of the void region area for both the systems with $a = 5.0$ is shown in Figs. 5(b,c). The distribution is taken with weighting by the void region area $S^{(\mathrm{void})}$. The distribution is narrower in the system with rhomboidal particles

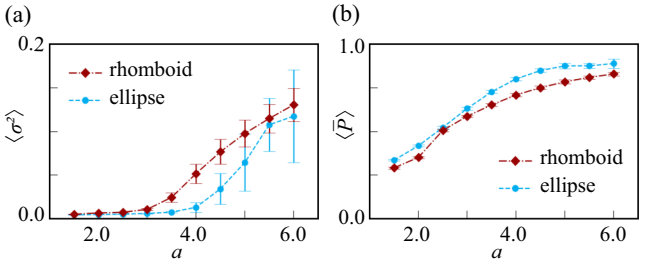

FIG. 6. Ensemble and time average of (a) the local number density variance $\langle \sigma^2 \rangle$ and (b) the local nematic order $\langle \bar{P} \rangle$. Error bars indicate standard deviation.

than that in the system with elliptical particles.

IV. DISCUSSION

Here, we focus on the emergence of the void regions depending on the particle shape and the aspect ratio. To discuss the character of the void regions quantitatively, we define the variance σ_t^2 of the local number density $\rho_{\boldsymbol{j},t}$ with respect to $\boldsymbol{j}$ at the time step t as

$$\sigma_t^2 = \frac{\sum_{\boldsymbol{j}} (\rho_{\boldsymbol{j},t} - \bar{\rho}_t)^2}{M_x M_y}, \tag{17}$$

where $\bar{\rho}_t$ is the mean of $\rho_{\boldsymbol{j},t}$ with respect to $\boldsymbol{j}$ at the time step t. $\langle \sigma^2 \rangle$ is defined as the mean of σ_t^2 with respect to t and the ten trials. Figure 6(a) shows that the local density variance $\langle \sigma^2 \rangle$ changes from $\langle \sigma^2 \rangle \sim 0$ to finite values at $a = 3.0$ and 4.0 in the systems with rhomboidal and elliptical particles, respectively. The transition in $\langle \sigma^2 \rangle$ corresponds to the emergence of the void regions as shown in Fig. 4. To discuss the relationship between the void region emergence and the particle orientational order, we define the mean local nematic order $\langle \bar{P} \rangle$ as the mean of $\bar{P}_t$ with respect to t and the ten trials, where $\bar{P}_t$ is the mean of $P_{\boldsymbol{j},t}$ with respect to $\boldsymbol{j}$ for the region with $\rho \geq 0.3\rho^{(\mathrm{sys})}$. Figure 6(b) shows that the local nematic order $\langle \bar{P} \rangle$ gradually increases with an increase in a both in the systems with rhomboidal and elliptical particles, even at the aspect ratio where $\langle \sigma^2 \rangle$ sharply increases at $a \sim 3.0$ for the systems with rhomboidal particles. This suggests that the change in the orientation order is not directly affected by the emergence of the void regions.

Figures 5(b,c) show that the distribution of $S^{(\mathrm{void})}$ with rhomboidal particles for $a = 5.0$ is narrower than that with elliptical particles. Figures 5(a,b,c) suggest that the systems with rhomboidal particles have characteristic void areas that correlate with the aspect ratio.

Figure 4 shows that some void regions have the winding numbers $\Psi_{m,t} = +1$. Seeing particle orientation around the void regions, many void regions with $\Psi_{m,t} = +1$ are surrounded by particles whose long-axes are along with the borders of these void regions as shown in Fig. 7. We consider the size of the void regions may be associated

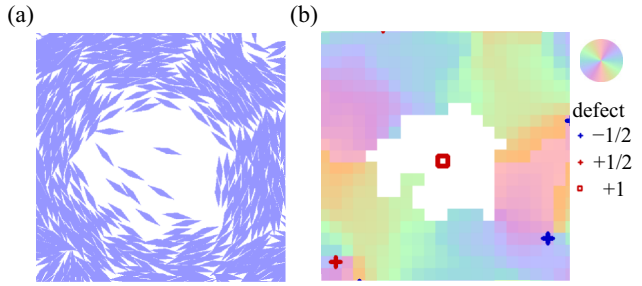

FIG. 7. Enlarged views around a void region with $\Psi_{m,t} = +1$ for the system with rhomboidal particles for $a = 5.0$, which are taken from (a) Fig. 1(a)(iii) and (b) Fig. 2(a). The area with 10×10 is shown.

with the particle orientation around them. To discuss the characteristic void area, we evaluate the orientational correlation lengths. They are calculated from a spatial correlation functions $C(r)$ of particle orientation which is defined as,

$$C(r) = \langle \cos 2(\theta_{i,t} - \theta_{i',t}) \rangle_{r<|\boldsymbol{x}_i - \boldsymbol{x}_{i'}|<r+\Delta r,t} . \tag{18}$$

Here, $\langle \cdot \rangle_{r<|\boldsymbol{x}_i - \boldsymbol{x}_{i'}|<r+\Delta r,t}$ denotes the mean with respect to pairs of the i-th and i'-th $(i, i' = 1, \ldots, N)$ particles with distances $r < |\boldsymbol{x}_i - \boldsymbol{x}_{i'}| < r + \Delta r$. The correlation length of the particle orientation $\lambda_{(\mathrm{C})}$ is defined as the minimum length r that satisfies $C(r) < e^{-1}$. The spatial correlation of the particle orientation for the particle pairs located around the same void regions $C^{(\mathrm{void})}(r)$ is also defined as

$$C^{(\mathrm{void})}(r) = \langle \cos 2(\theta_{i,t} - \theta_{i',t}) \rangle_{\{r<|\boldsymbol{x}_i - \boldsymbol{x}_{i'}|<r+\Delta r \,|\, i,i' \in \boldsymbol{\mathcal{P}}_{m,t}\},t} . \tag{19}$$

Here, $\boldsymbol{\mathcal{P}}_{m,t}$ is the set of the indices of the two particles whose distances from void points belonging to the m-th void region are both less than $+1$ at the time step t. $\langle \cdot \rangle_{\{r<|\boldsymbol{x}_i - \boldsymbol{x}_{i'}|<r+\Delta r \,|\, i,i' \in \boldsymbol{\mathcal{P}}_{m,t}\},t}$ denotes the mean of the values for the particle pairs, both of which are the elements of $\boldsymbol{\mathcal{P}}_{m,t}$ and whose distances are $r < |\boldsymbol{x}_i - \boldsymbol{x}_{i'}| < r + \Delta r$. The correlation length $\lambda_{(\mathrm{C})}^{(\mathrm{void})}$ of particle orientation is defined as the minimum length r that satisfies $C^{(\mathrm{void})}(r) < e^{-1}$. Figure 8 shows $C(r)$, $C^{(\mathrm{void})}(r)$, $\lambda_{(\mathrm{C})}$, and $\lambda_{(\mathrm{C})}^{(\mathrm{void})}$ for both the systems with rhomboidal and elliptical particles. $\lambda_{(\mathrm{C})}$ and $\lambda_{(\mathrm{C})}^{(\mathrm{void})}$ increase with an increase in a in both the systems.

Considering the alignment of the particles surrounding the void regions, we estimate void areas $S_{(\mathrm{C})}^{(\mathrm{void})}$ from $\lambda_{(\mathrm{C})}^{(\mathrm{void})}$ for each a. Figure 9(a) shows the schematic illustration for the definition of $S_{(\mathrm{C})}^{(\mathrm{void})}$. Here, we expect the angle difference between two particles with a distance of $\lambda_{(\mathrm{C})}^{(\mathrm{void})}$ along the void border is $\left(\arccos\left(e^{-1}\right)\right)/2$ considering the definition of the correlation length. Then, the

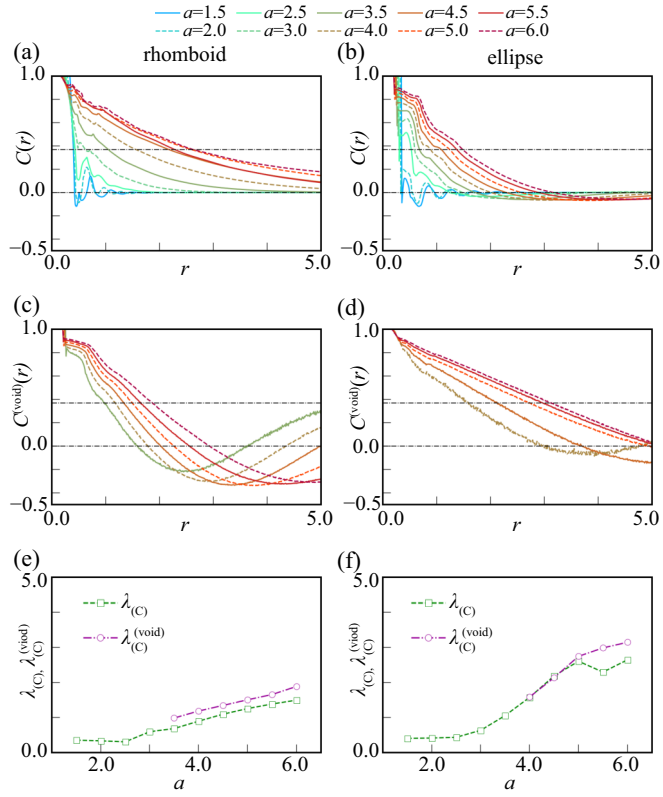

FIG. 8. (a,b) Spatial correlation of the particle orientation $C(r)$ in the whole region for the system with (a) rhomboidal and (b) elliptical particles. (c,d) Spatial correlation of the particle orientation for particle pairs located around the same void regions $C^{(\mathrm{void})}(r)$ for the system with (c) rhomboidal and (d) elliptical particles. (e,f) Correlation lengths in the whole region $\lambda_{(\mathrm{C})}$ and those for particle pairs located around the same void regions $\lambda_{(\mathrm{C})}^{(\mathrm{void})}$ depending on the aspect ratio a for the systems with (e) rhomboidal and (f) elliptical particles.

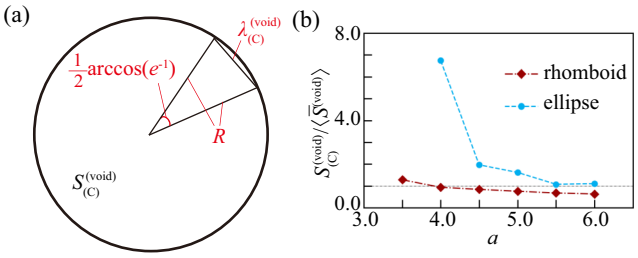

FIG. 9. (a) Schematic illustration for the estimation of void sizes $S_{(\mathrm{C})}^{(\mathrm{void})}$ from $\lambda_{(\mathrm{C})}^{(\mathrm{void})}$. The void region is considered as a circumscribed circle surrounded by edges whose length is given as the orientational correlation length. The radius R of the void region is calculated as in Eq. (21). (b) Ratio $S_{(\mathrm{C})}^{(\mathrm{void})} / \left\langle \bar{S}^{(\mathrm{void})} \right\rangle$ against a.

void areas $S_{(\mathrm{C})}^{(\mathrm{void})}$ are estimated as

$$S_{(\mathrm{C})}^{(\mathrm{void})} = \pi \left(R_{(\mathrm{C})}^{(\mathrm{void})} \right)^2, \tag{20}$$

where

$$R_{(\mathrm{C})}^{(\mathrm{void})} = \frac{2\pi \lambda_{(\mathrm{C})}^{(\mathrm{void})}}{\arccos\left(e^{-1}\right)/2}. \tag{21}$$

Figure 9(b) shows $S_{(\mathrm{C})}^{(\mathrm{void})} / \left\langle \bar{S}^{(\mathrm{void})} \right\rangle$ against a for the comparison between the observed mean void area and the estimated one. The ratio for rhomboidal particles is almost constant, while that for elliptical particles greatly varies depending on a. In addition, it should be mentioned that the systems with rhomboidal particles include more void regions with $\Psi_{m,t} = +1$ than those with elliptical particles. These results suggest that the void areas in the systems with rhomboidal particles could be directly determined by the orientational correlation length.

V. CONCLUSION

We simulated a model of active nematics, in which rhomboidal or elliptical particles interact by direct collision, and investigated by varying the particle aspect ratio to observe the correlation between the collective pattern and the particle shape. The local density variance and the local nematic orientation increase with an increase in the aspect ratio both in the systems with rhomboidal particles and elliptical particles. The void regions where the particle number density is almost zero appear only for high aspect ratios in both the systems. The systems with rhomboidal particles have the characteristic void size, which has a positive correlation with the aspect ratio, while the systems with elliptical particles do not have the clear characteristic void size and show a broad size distribution. Most void regions are surrounded by particles whose long-axes are along with the borders of the void regions in the systems with rhomboidal particles. Considering the proportionality between the observed void area and the void area estimated from the orientational correlation length, the size of the void regions might be determined by the particle shape and the aspect ratio through the difference in the orientational correlation length.

ACKNOWLEDGMENTS

This work was supported by JST SPRING, Grant Number JPMJSP2109 (MS), by JSPS KAKENHI Grant Nos. JP21K13891 (HI), JP20H02712, JP21H00996, and JP21H01004 (HK), and by the Cooperative Research Program of "NJRC Mater. & Dev." No.20224003 (HK).

[1] G. Gompper, R. G. Winkler, T. Speck, A. Solon, C. Nardini, F. Peruani, H. Löwen, R. Golestanian, U. B. Kaupp, L. Alvarez, T. Kiorboe, E. Lauga, W. C. K. Poon, A. DeSimone, S. M. nos Landin, A. F. N. A. Söker, F. Cichos, R. Kapral, P. Gaspard, M. Ripoll, F. F. Sagués, A. Doostmohammadi, J. M. Yeomans, I. S. Aranson, C. Bechinger, H. Stark, C. K. Hemelrijk, F. J. Nedelec, T. Sarkar, T. Aryaksama, M. Lacroix, G. Duclos, V. Yashunsky, P. Silberzan, M. Arroyo, and S. Kale, J. Phys. **32**, 193001 (2020).
[2] M. Das, C. F. Schmidt, and M. Murrell, Soft Matter **16**, 7185 (2020).
[3] T. Vicsek and A. Zafeiris, Phys. Rep. **517**, 71 (2012).
[4] S. Ramaswamy, R. A. Simha, and J. Toner, E.P.L. **62**, 196 (2003).
[5] S. Ramaswamy, Annu. Rev. Condens. Matter Phys. **1**, 323 (2010).
[6] V. Narayan, S. Ramaswamy, and N. Menon, Science **317**, 105 (2007).
[7] M. E. Cates and J. Tailleur, Annu. Rev. Condens. Matter Phys. **6**, 219 (2015).
[8] M. R. Shaebani, A. Wysocki, R. G. Winkler, G. Gompper, and H. Rieger, Nat. Rev. Phys. **2**, 181 (2020).
[9] M. E. Cates and J. Tailleur, EPL **101**, 20010 (2013).
[10] Y. Fily and M. C. Marchetti, Phys. Rev. Lett. **108**, 235702 (2012).
[11] S. Shankar, A. Souslov, M. J. Bowick, M. C. Marchetti, and V. Vitelli, Nat. Rev. Phys. **4**, 380 (2022).
[12] W. Wang, W. Duan, S. Ahmed, A. Sen, and T. E. Mallouk, Acc. Chem. Res. **48**, 1938 (2015).
[13] V. N. Manoharan, Science **349**, 6251 (2015).
[14] M. C. Marchetti, Y. Fily, S. Henkes, A. Patch, and D. Yllanes, Curr. Opin. Colloid Interface Sci. **21**, 34 (2016).
[15] J. Stenhammar, R. Wittkowski, D. Marenduzzo, and M. E. Cates, Phys. Rev. Lett. **114**, 018301 (2015).
[16] M. C. Marchetti, J. F. Joanny, S. Ramaswamy, T. B. Liverpool, J. Prost, M. Rao, and R. A. Simha, Rev. Mod. Phys. **85**, 1143 (2013).
[17] S. C. Takatori, R. D. Dier, J. Vermant, and J. F. Brady, Nat. Commun. **7**, 10694 (2016).
[18] J. Zhang, B. A. Grzybowski, and S. Granick, Langmuir **33**, 6964 (2017).
[19] J. Palacci, S. Sacanna, A. P. Steinberg, D. J. Pine, and P. M. Chaikin, Science **339**, 936 (2013).
[20] T. Vicsek, A. Czirók, E. Ben-Jacob, I. Cohen, and O. Shochet, Phys. Rev. Lett. **75**, 1226 (1995).
[21] F. Ginelli, Eur. Phys. J. Spec. Top. **225**, 2099 (2016).
[22] A. Doostmohammadi, J. Ignés-Mullol, J. M. Yeomans, and F. Sagués, Nat. Commun. **9**, 3246 (2018).
[23] L. Balasubramaniam, R.-M. Mège, and B. Ladoux, Curr. Opin. Genet. Dev. **73**, 101897 (2022).
[24] T. Sanchez, D. T. N. Chen, S. J. DeCamp, M. Heymann, and Z. Dogic, Nature **491**, 431 (2012).
[25] L. M. Lemma, S. J. DeCamp, Z. You, L. Giomi, and Z. Dogic, Soft Matter **15**, 3264 (2019).

[26] T. Strübing, A. Khosravanizadeh, A. Vilfan, E. Bodenschatz, R. Golestanian, and I. Guido, Nano Lett. **20**, 6281 (2020).

[27] D. D. Arciprete, M. L. Blow, A. T. Brown, F. D. C. Farrell, J. S. Lintuvuori, A. F. McVey, D. Marenduzzo, and W. C. K. Poon, Nat. Commun. **9**, 4190 (2018).

[28] H. Lia, X. Q. Shi, M. Huanga, X. Chena, M. Xiaoe, C. Liue, H. Chate, and H. P. Zhanga, Proc. Natl. Acad. Sci. U.S.A. **116**, 777 (2018).

[29] M. M. Genkin, A. Sokolov, O. D. Lavrentovich, and I. S. Aranson, Phys. Rev. X **7**, 011029 (2017).

[30] M. L. Blow, M. Aqil, B. Liebchena, and D. Marenduzzo, Soft Matter **13**, 6137 (2017).

[31] Y. I. Yaman, E. Demir, R. Vetter, and A. Kocabas, Nat. Commun. **10**, 2285 (2019).

[32] A. Doostmohammadi, S. P. Thampi, T. B. Saw, C. T. Lim, B. Ladoux, and J. M. Yeomans, Soft Matter **11**, 7328 (2015).

[33] L. S. Hirst and G. Charras, Nature **544**, 164 (2017).

[34] A. Tijore, S. A. Irvine, U. Sarig, P. Mhaisalkar, V. Baisane, and S. Venkatraman, Biofabrication **10**, 025003 (2018).

[35] T. Turiv, J. Krieger, G. Babakhanova, H. Yu, S. V. Shiyanovskii, Q.-H. Wei, M.-H. Kim, and O. D. Lavrentovich, Sci. Adv. **6**, eaaz6485 (2020).

[36] B. Liebchen and D. Levis, EPL **139**, 67001 (2022).

[37] Q.-L. Lei, M. P. Ciamarra, and R. Ni, Sci. Adv. **5**, eaau7423 (2019).

[38] B. Liebchen and D. Levis, Phys. Rev. Lett. **119**, 058002 (2017).

[39] P. Guillamat, J. Ignés-Mullol, and F. Sagués, Proc. Natl. Acad. Sci. U.S.A. **113**, 5498 (2016).

[40] S. J. DeCamp, G. S. Redner, A. Baskaran, M. F. Hagan, and Z. Dogic, Nat. Mater. **14**, 1110 (2015).

[41] S. P. Thampi, R. Golestanian, and J. M. Yeomans, EPL **105**, 18001 (2014).

[42] S. P. Thampi, A. Doostmohammadi, R. Golestanian, and J. M. Yeomans, EPL **112**, 28004 (2015).

[43] S. Henkes, M. C. Marchetti, and R. Sknepnek, Phys. Rev. E **97**, 042605 (2018).

[44] R. Zhang, N. Kumar, J. L. Ross, and J. J. de Pablo, Proc. Natl. Acad. Sci. U.S.A. **115**, E124 (2017).

[45] C. Blanch-Mercader, V. Yashunsky, S. Garcia, G. Duclos, L. Giomi, and P. Silberzan, Phys. Rev. Lett. **120**, 208101 (2018).

[46] S. Zhou, A. Sokolov, O. D. Lavrentovich, and I. S. Aranson, Proc. Natl. Acad. Sci. U.S.A. **111**, 1265 (2014).

[47] H. Chaté, F. Ginelli, and R. Montagne, Phys. Rev. Lett. **96**, 180602 (2006).

[48] S. Weitz, A. Deutsch, and F. Peruani, Phys. Rev. E **92**, 012322 (2015).

[49] F. Peruani, A. Deutsch, and M. Bär, Phys. Rev. E **74**, 030904(R) (2006).

[50] S. Mishra and S. Ramaswamy, Phys. Rev. Lett. **97**, 090602 (2006).

[51] L. Giomi, Mark, J. Bowick, P. Mishra, R. Sknepnek, and M. C. Marchetti, Phil. Trans. R. Soc. A. **372**, 20130365 (2014).

[52] M. M. Genkin, A. Sokolov, O. D. Lavrentovich, and I. S. Aranson, Phys. Rev. X **7**, 011029 (2017).

[53] V. Schaller and A. R. Bausch, Proc. Natl. Acad. Sci. U.S.A. **110**, 4488 (2013).

[54] K. Kawaguchi, R. Kageyama, and M. Sano, Nature **545**, 327 (2017).

[55] I. S. Aranson, Acc. Chem. Res. **51**, 3023 (2018).

[56] X. Q. Shi and Y. Q. Ma, Nat. Commun. **4**, 2013 (2013).

[57] S. E. Moran, I. R. Bruss, P. W. A. Schönhöfer, and S. C. Glotzer, Soft Matter **18**, 1044 (2022).

[58] S. E. Moran, P. W. A. Schönhöfer, and S. C. Glotzer, New J. Phys. **24**, 063007 (2022).